Contrast-Enhanced X-ray Detection of Breast Microcalcifications in a Murine Model Using Targeted Gold Nanoparticles

Lisa E. Cole,[†,‡] Tracy Vargo-Gogola,[§,‡] and Ryan K. Roeder[†,‡,*]

[†]Department of Aerospace and Mechanical Engineering, Bioengineering Graduate Program and [‡]Harper Cancer Research Institute, University of Notre Dame, Notre Dame, Indiana 46556, United States and [§]Department of Biochemistry and Molecular Biology, Indiana University Simon Cancer, Center Indiana University School of Medicine — South Bend, South Bend, Indiana 46617, United States

ABSTRACT Microcalcifications are deposits of hydroxyapatite (HA) mineral within breast tissue and the most common abnormality detected by mammography when screening for breast cancer due to exhibiting greater X-ray attenuation than the surrounding tissue. However, the detection of microcalcifications is limited by the sensitivity and specificity of mammography. Therefore, the objective of this study was to investigate *in vivo* targeted delivery of bisphosphonate-functionalized gold nanoparticles (BP-Au NPs) for contrast-enhanced detection of microcalcifications using computed tomography (CT). A murine model was developed for precise, *a priori* control over the level of microcalcification burden by injecting varying concentrations of HA crystals in a Matrigel carrier into mammary glands. The measured X-ray attenuation of microcalcifications containing varying HA concentrations demonstrated that the model was reproducible and able to recapitulate varying levels of microcalcification burden, including levels undetectable by CT in the absence of contrast enhancement. After intramammary delivery, BP-Au NPs provided enhanced contrast for the detection of microcalcifications that were otherwise below the CT detection limit. BP-Au NPs targeted microcalcifications due to specific binding to HA crystal surfaces, resulting in contrast between the HA microcalcification site and surrounding tissue which was visibly apparent (~30−135 HU) within 2 days after delivery. Therefore, targeted BP-Au NPs enabled improved sensitivity and specificity for the detection of microcalcifications.

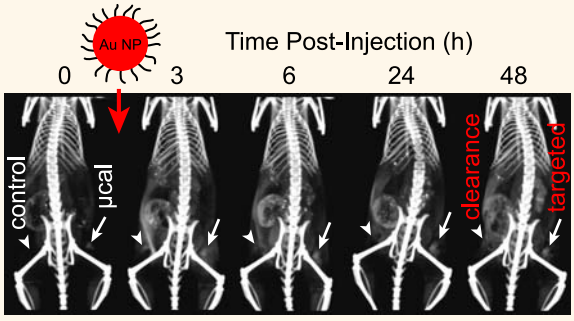

KEYWORDS: breast cancer · computed tomography · contrast agent · gold nanoparticles · microcalcification · targeted delivery · X-ray imaging

Early detection is one of the most important aspects of cancer management as a proven means to decrease mortality.[1] Primary tumors must be detected in the earliest stages before spreading to metastatic disease in order for treatments to be effective.[1] The five-year survival rate of patients with a tumor confined to the breast tissue is 98.6%, but only 23.3% when the cancer has metastasized to distant sites.[2] Biomedical imaging has proven to be beneficial in the management of many different cancers, particularly in early detection and diagnosis.[3]

Mammography is highly effective in screening for early detection of breast cancer[4] with a demonstrated reduction in mortality up to 30%.[5,6] Mammography utilizes a low-dose of X-rays to visualize the breast tissue and screen for abnormalities *in vivo*. Microcalcifications are the most common abnormality detected by mammography;[7] 30−50% of all nonpalpable breast cancers are detected on the basis of the finding of a microcalcification on a mammogram.[7−9] Thus, breast microcalcifications are an important early marker for breast cancer. Microcalcifications are deposits of hydroxyapatite (HA) and calcium oxalate mineral within the breast tissue,[10−12] which exhibit high X-ray attenuation compared to the surrounding soft tissue. However, the detection of microcalcifications and other breast lesions is currently limited by the sensitivity and specificity

* Address correspondence to rroeder@nd.edu.

Received for review May 21, 2014 and accepted July 3, 2014.

Published online July 03, 2014
10.1021/nn5027802

of mammography. Microcalcifications can be missed due to a small size (0.1−1.0 mm) or low mineral density, while other structures of the breast, such as fibrous tissue, ducts, and blood vessels, can be mistaken as microcalcifications due to exhibiting a relatively high X-ray attenuation compared to the surrounding adipose tissue.[8] Therefore, improvements are needed for the detection of microcalcifications using X-ray imaging during breast cancer screening.

Gold nanoparticles (Au NPs) have gained attention as a potential X-ray contrast agent due to exhibiting greater X-ray attenuation and longer vascular retention times compared to iodinated molecular agents.[13−15] Au NPs are readily synthesized and surface functionalized for colloidal stability and targeted delivery.[16] Au NPs have also been shown to be noncytotoxic *in vivo* at the concentrations necessary for contrast enhancement.[13−15] Au NPs surface functionalized with tumor-specific biomarkers have demonstrated potential as a targeted X-ray contrast agent for cancer cells *in vitro*[17−20] and tumors *in vivo*.[21−28] In a number of *in vivo* studies, targeted labeling of a tumor with Au NPs led to enhanced contrast of the tumor compared to surrounding tissue, demonstrating the possibility of improved early detection of tumors otherwise undetectable by X-ray imaging.[21−28]

Bisphosphonate-functionalized gold nanoparticles (BP-Au NPs) (Figure 1a) were recently introduced as a potential targeted X-ray contrast agent for breast microcalcifications.[29] Bisphosphonates, such as alendronate, exhibit high binding affinity for hydroxyapatite (HA) and may therefore be used to target microcalcifications. BP-Au NPs exhibited colloidal stability in physiologic media[30] and high binding affinity for HA crystals *in vitro*.[31] BP-Au NPs enabled contrast-enhanced detection of microcalcifications in an *in vitro* imaging phantom and *ex vivo* tissue model of breast microcalcifications.[29] Model microcalcifications comprising HA crystals that were labeled by BP-Au NPs exhibited significantly greater X-ray attenuation compared to unlabeled HA crystals at the same concentration, including at microcalcification levels that were otherwise below the X-ray detection limit. However, HA crystals were labeled by BP-Au NPs *in vitro*, which represents a best-case scenario compared to *in vivo* delivery. Targeted delivery of BP-Au NPs *in vivo* may be hindered by competitive protein binding on microcalcifications, and only a small fraction of the initial dose may reach the microcalcification.

Therefore, the objective of this study was to investigate the *in vivo* targeted delivery of BP-Au NPs for contrast-enhanced detection of microcalcifications using CT. A murine model of microcalcifications was developed to allow for precise, *a priori* control of the level of mineral deposits within mammary glands (Figure 1b). The model was first characterized *in vivo* by measuring changes in X-ray attenuation due to various levels of microcalcification burden using a preclinical CT at a clinically relevant resolution, including after labeling microcalcifications with different doses of BP-Au NPs *in vitro*. The murine model was subsequently used to investigate *in vivo* targeted delivery of BP-Au NPs and contrast-enhanced detection of microcalcifications (Figure 1c).

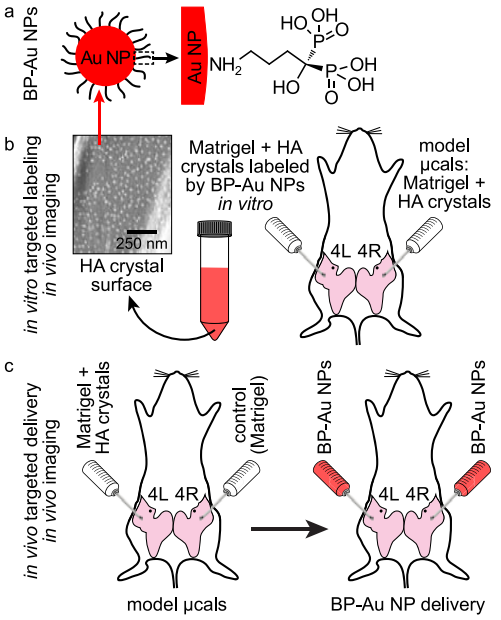

Figure 1. Schematic illustration of the experimental design. (a) Au NPs were surface-functionalized with alendronate, a bisphosphonate with a primary amine for binding gold surfaces opposite phosphonate groups for targeting calcium ions on HA crystal surfaces. (b) A murine model was developed for precise, *a priori* control over the level of microcalcification (*µ*cal) burden by injecting varying concentrations of HA crystals in a Matrigel carrier into mammary glands *in vivo*. HA crystals were also labeled by BP-Au NPs *in vitro*, prior to mixing with Matrigel, in order in characterize the detection limits and the effect of the dose of BP-Au NPs prior to investigating *in vivo* targeted delivery. (c) The murine model was subsequently used to investigate *in vivo* targeted delivery of BP-Au NPs and contrast-enhanced detection of microcalcifications.

RESULTS AND DISCUSSION

Characterization of BP-Au NPs. BP-Au NPs were synthesized using the citrate reduction method and surface functionalized with alendronate, which provided a primary amine for binding to the Au NP surface opposite phosphonate groups for targeting HA crystals (Figure 1a). As-synthesized BP-Au NPs were concentrated to 50 mM (9.8 mg/mL) by centrifugation prior to subsequent *in vivo* delivery. BP-Au NPs in concentrated solutions remained spherical and monodispersed (Figure 2a) with a mean (±standard deviation) diameter of 12.3 (1.2) nm as measured by TEM (Figure 2b). Colloidal stability after concentrating BP-Au NPs was verified using dynamic light scattering (DLS) and UV−vis spectroscopy; the mean (±standard deviation) hydrodynamic diameter was 48.6 (1.2) nm (Figure 2b),

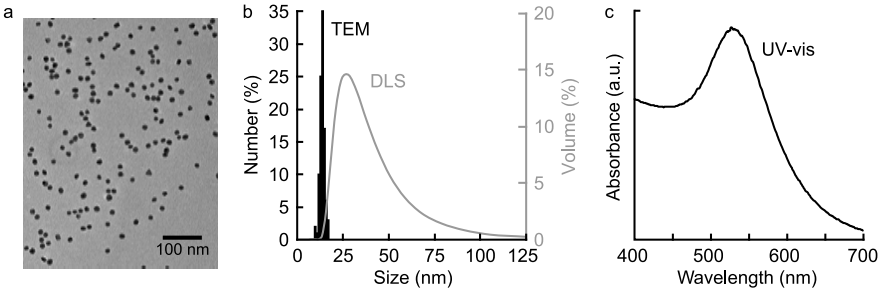

Figure 2. Characterization of BP-Au NPs concentrated by centrifugation for subsequent *in vivo* delivery. (a) Representative TEM micrograph showing spherical and monodispersed BP-Au NPs. (b) Size distributions showing the physical diameter measured by TEM and the hydrodynamic diameter measured by DLS. (c) UV−vis spectra of BP-Au NPs showing the surface plasmon resonance peak at ∼527 nm.

and the characteristic surface plasmon resonance peak was observed at ∼527 nm (Figure 2c), respectively. These results were consistent with previously published results for ∼13 nm BP-Au NPs.[29−31] Therefore, the size and colloidal stability of BP-Au NPs were not altered by the repetitive centrifugation necessary to concentrate the BP-Au NPs. As-synthesized BP-Au NPs were also previously shown to exhibit colloidal stability in phosphate buffered saline and fetal bovine serum for at least 7 days,[30] and the bisphosphonate surface density was measured to be ∼3.5 molecules/nm^2.[32]

Murine Model of Breast Microcalcifications. A murine model of microcalcifications was developed to allow for precise, *a priori* control of the level of mineral deposits within mammary glands (MGs) *in vivo*. HA crystals were mixed in a Matrigel carrier at varying concentrations (0, 0.5, 5.0, 25 mg/mL) and injected into the fat pad of the right number 4 MG in anesthetized mice (Figure 1b). The X-ray attenuation of HA microcalcifications increased with increasing HA concentration ($p < 0.0001$, $R^2 > 0.96$, ANOVA) (Figure 3), demonstrating that the model was reproducible and able to recapitulate varying levels of microcalcification burden. Microcalcifications containing 5 and 25 mg/mL HA exhibited significantly greater X-ray attenuation compared to Matrigel controls ($p < 0.01$, *t*-test). Differences in X-ray attenuation between microcalcifications containing 0.5 mg/mL HA and Matrigel controls were not statistically different ($p > 0.30$, *t*-test); therefore, microcalcifications containing 0.5 mg/mL HA were established as undetectable by X-ray imaging in the absence of contrast enhancement.

Planar radiographs were used to confirm the location of microcalcifications within the fat pad of MGs, as well as the relative size and shape of each microcalcification (Figure 4a). The placement of microcalcifications was guided using the nipple of the number 4 MG as an anatomic landmark for HA-Matrigel injections, mitigating the need for a more invasive surgery. The observed location of microcalcifications relative to the lymph nodes (Figure 4a) confirmed that this minimally invasive procedure provided accurate and repeatable placement of microcalcifications in MGs. An increase in

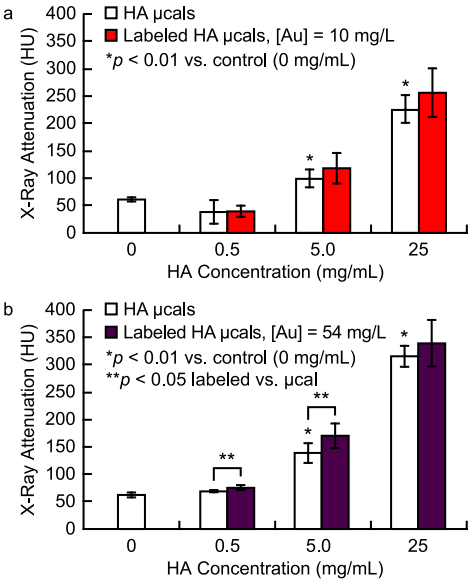

Figure 3. X-ray attenuation (HU) measured *in vivo* by CT for microcalcifications (μcals) created by injecting varying concentrations of HA crystals within a Matrigel carrier into murine MGs, including HA crystals labeled by (a) 10 and (b) 54 mg/L BP-Au NP solutions *in vitro*. Error bars show one standard deviation of the mean. The X-ray attenuation of HA microcalcifications increased with increasing HA concentration ($p < 0.0001$, $R^2 > 0.96$, ANOVA). Microcalcifications containing 5.0 and 25 mg/mL HA exhibited greater X-ray attenuation compared to the Matrigel control (0 mg/mL) (*$p < 0.01$, *t*-test), but the lowest HA concentration (0.5 mg/mL) was undetectable compared to the Matrigel control (0 mg/mL) ($p > 0.30$, *t*-test) in the absence of contrast enhancement. (a) Labeling by BP-Au NPs did not result in increased X-ray attenuation of microcalcifications at any HA concentration when HA crystals were exposed to a lower dose (10 mg/L) of BP-Au NPs ($n = 3$/group). (b) BP-Au NPs enhanced the X-ray attenuation of microcalcifications containing 0.5 and 5.0 mg/mL HA when HA crystals were exposed to a higher dose (54 mg/L) of BP-Au NPs ($p < 0.05$, paired *t*-test) ($n = 5$/group).**

the size and X-ray attenuation of microcalcifications was visibly apparent with increasing HA concentration (Figure 4a), further demonstrating that the model was able to recapitulate varying levels of microcalcification burden.

The *in vivo* murine model of microcalcifications developed in this study was an extension of an

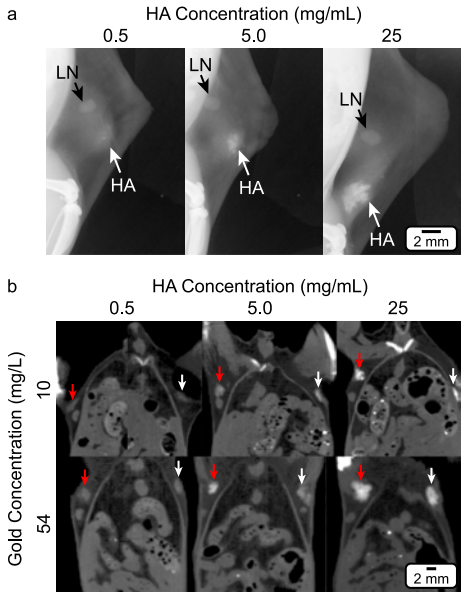

Figure 4. Representative (a) planar radiographs and (b) gray scale CT images showing HA microcalcifications (white arrows) and HA microcalcifications labeled by BP-Au NPs (red arrows) within murine MGs *in vivo*. (a) Planar radiographs were used to confirm the location of HA microcalcifications (white arrows) within the fat pad of the number 4 MG. The lymph node (LN, black arrows) was used as an anatomic landmark for imaging. The size and X-ray attenuation of microcalcifications was visibly increased with increasing HA concentration, modeling a change in the microcalcification burden. (b) Gray-scale CT images showed that contrast enhancement was visibly apparent for microcalcifications containing 5.0 mg/mL HA when labeled by 54 mg/L BP-Au NPs *in vitro*.

ex vivo tissue model we previously reported.[29] Other *in vivo* models of breast microcalcifications have been previously developed in rodents using implanted tumor cells[33] and exogenous growth factors.[34−36] These models are more biologically relevant for the spontaneous formation and growth of microcalcifications, but the amount of mineral that is deposited varies between animals and requires additional verification. Furthermore, the formation of microcalcifications in these models is preceded by tumor formation, in contrast to the normal disease progression, and the presence of tumor tissue may create additional model variability due to differences in the X-ray attenuation of the background tissue between animals. For these reasons, the model developed in this study was advantageous for quantitative assessment of contrast-enhanced CT due to enabling precise, *a priori* control over the level of microcalcification burden in mouse MGs using a minimally invasive procedure.

***In Vivo* Contrast-Enhanced Detection of Microcalcifications Labeled by BP-Au NPs *in Vitro*.** The murine model of microcalcifications was further characterized by measuring changes in X-ray attenuation due to labeling microcalcifications with BP-Au NPs using a preclinical CT at a clinically relevant resolution. HA crystals were labeled by two doses of BP-Au NPs (10 and 54 mg/L) *in vitro* prior to being mixed in the Matrigel carrier at varying concentrations (0, 0.5, 5.0, 25 mg/mL), injected into the fat pad of the left number 4 MG of the same mice used to characterize the model as described above (Figure 1b), and imaged by CT *in vivo*. Labeling the HA crystals *in vitro* was deemed a beneficial preliminary step to characterize the detection limit for contrast-enhanced CT and the effects of the BP-Au NP dose while avoiding potential complications associated with *in vivo* delivery. Two doses of BP-Au NPs (10 and 54 mg/L) were chosen to lead to differences in the surface density or mass concentration of BP-Au NPs labeling HA crystals based upon prior knowledge of the equilibrium binding.[31,32]

BP-Au NPs enabled contrast-enhanced detection of microcalcifications by CT *in vivo* when the HA crystals were labeled by a sufficiently high dose of BP-Au NPs *in vitro*. Labeling by BP-Au NPs did not result in increased X-ray attenuation of microcalcifications at any HA concentration when HA crystals were exposed to a lower dose (10 mg/L) of BP-Au NPs ($p > 0.19$, paired *t*-test) (Figure 3a). However, BP-Au NPs enhanced the X-ray attenuation of microcalcifications containing 0.5 and 5.0 mg/mL HA when HA crystals were exposed to a higher dose (54 mg/L) of BP-Au NPs ($p < 0.05$, paired *t*-test) (Figure 3b). Thus, BP-Au NPs enabled detection of microcalcifications (0.5 mg/mL HA) that were otherwise below the CT detection limit. The measured differences in X-ray attenuation were visibly apparent in gray-scale CT images for microcalcifications containing 5.0 mg/mL HA (Figure 4b).

Contrast-enhanced detection required that HA crystals within microcalcifications were exposed to a sufficiently high initial dose of BP-Au NPs (Figure 3). Therefore, the percent of the BP-Au NP dose bound to HA and the mass of BP-Au NPs bound per mass of HA were measured to investigate the effects of the initial BP-Au NP dose and HA concentration on HA binding. Complete binding occurred at HA concentrations of 5.0 and 25 mg/mL for either dose of BP-Au NPs, and the percent binding was significantly lower ($p < 0.05$, *t*-test) for the higher BP-Au NP dose at a HA concentration of 0.5 mg/mL due to an excess dose for the available HA surface area (Figure 5a). However, the mass of BP-Au NPs bound per mass of HA (mg Au/g HA) was significantly greater for the higher dose compared to lower dose of BP-Au NPs at each HA concentration ($p < 0.05$, *t*-test) and decreased with increasing HA concentration for either dose ($p < 0.0001$, ANOVA) (Figure 5b). Thus, the higher initial dose was able to drive equilibrium surface adsorption toward a greater mass of BP-Au NPs bound per mass of HA crystals, which led to an increase in X-ray attenuation (Figure 3). In other words, the mass of Au bound to HA crystals exposed to the lower dose of BP-Au NPs was insufficient for contrast enhancement, indicating that a sufficiently high mass concentration of Au must be delivered and bound to

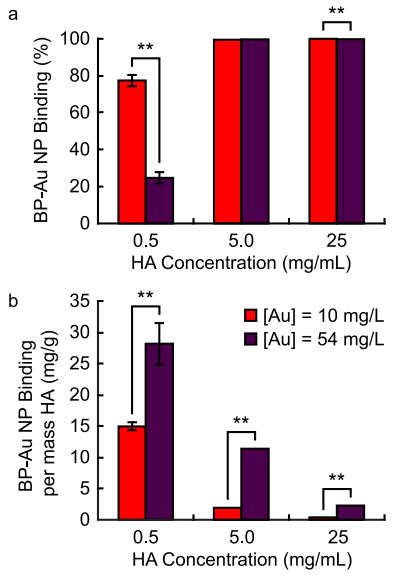

Figure 5. BP-Au NP binding to varying concentrations of HA crystals *in vitro* was characterized by measuring the concentration of unbound BP-Au NPs using ICP-OES. Error bars show one standard deviation of the mean (n = 3/group), and error bars not shown were negligibly small. (a) Complete binding occurred at HA concentrations of 5.0 and 25 mg/mL for either dose of BP-Au NPs, and the percent binding was significantly lower (*p < 0.05, t-test) for the higher BP-Au NP dose at an HA concentration of 0.5 mg/mL due to an excess dose for the available HA surface area. (b) The mass of BP-Au NPs bound per mass of HA (mg Au/mg HA) was significantly greater for the higher dose compared to lower dose of BP-Au NPs at each HA concentration (*p < 0.05, t-test), and decreased with increasing HA concentration for either BP-Au NP dose (p < 0.0001, ANOVA).

microcalcifications to enable contrast enhancement. Numerous imaging phantom and *in vitro* targeted delivery studies have shown a linear increase in X-ray attenuation with increased mass concentration of Au NPs.[14,15,24−28,32] Therefore, delivering a high mass concentration of Au to the targeted site is of primary importance for contrast-enhanced CT.[32]

CT and X-ray attenuation measurements utilized a small animal preclinical CT scanner (Albira, Bruker) with 125 μm resolution. This resolution was lower than commercially available micro-CT systems but similar to the resolution of clinical mammography[37] and breast CT[38] imaging systems in order to evaluate translational potential. As described above, contrast-enhanced detection required delivery of a sufficiently high mass concentration of BP-Au NPs targeting the microcalcification. However, the minimum mass concentration of Au required for contrast-enhanced detection is also dependent on the imaging system and resolution. In a previous study using micro-CT at 10 and 100 μm resolution, we reported that BP-Au NPs enabled contrast-enhanced detection of HA microcalcifications in an *ex vivo* tissue model when HA crystals were exposed to the same lower dose (10 mg/L) of BP-Au NPs that did not enhance contrast in the present study.[29] Therefore, it is important to evaluate dosing and translational potential using a clinically relevant imaging resolution because detection limits are dependent on the imaging system.[39]

A differential contrast (ΔHU) of at least 30 HU has been suggested to be necessary for visibly apparent enhanced-contrast in clinical CT.[39,40] Microcalcifications containing 5.0 mg/mL HA exhibited a differential contrast of ~30 HU after HA crystals were labeled with the higher dose (54 mg/L) of BP-Au NPs (Figure 3b) and enhanced-contrast was visibly apparent in gray-scale CT images (Figure 4b). Microcalcifications containing 0.5 mg/mL HA also exhibited a statistically significant increase in X-ray attenuation after labeling with the higher dose of BP-Au NPs (Figure 3b), but the differential contrast was only ~7 HU, due to a smaller mass of Au in the HA-Matrigel mixture, and was not readily apparent in gray-scale CT images (Figure 4b). Therefore, contrast-enhanced detection of microcalcifications containing a low concentration of HA (0.5 mg/mL) was determined to require a greater initial dose of BP-Au NPs than that used in this experiment (54 mg/L or 0.27 mM). In subsequent experiments investigating *in vivo* targeted delivery, the concentration of BP-Au NPs administered was increased to 50 mM, which corresponded to a total dose of 2.0 mg Au available for HA binding *in vivo* compared to 0.86 mg Au that was available for binding to HA crystals *in vitro*.

***In Vivo* Targeted Delivery of BP-Au NPs for Contrast-Enhanced Detection of Microcalcifications.** The murine model of microcalcifications was used to investigate targeted delivery of BP-Au NPs by intramammary injection (Figure 1c) and contrast-enhanced detection of microcalcifications by measuring longitudinal changes in X-ray attenuation. Based on the preceding characterization of the model, two HA concentrations were chosen to mimic two levels of microcalcification burden and model two clinically relevant scenarios. (1) Microcalcifications containing 0.5 mg/mL HA were shown to be undetectable by CT in the absence of contrast enhancement and were therefore used here to investigate improved sensitivity by contrast-enhanced imaging. (2) Microcalcifications containing 5.0 mg/mL HA were shown to be detectable by CT in the absence of contrast enhancement and were therefore used here to investigate improved specificity by contrast-enhanced imaging. Left MGs were injected with HA-Matrigel mixtures to model microcalcifications and right MGs were injected with Matrigel alone as a contralateral control to demonstrate targeting of BP-Au NPs to HA and imaging specificity.

The difference in X-ray attenuation exhibited by microcalcifications containing 0.5 mg/mL HA and Matrigel controls was not statistically significant (p = 0.85, paired t-test), confirming that these microcalcifications were undetectable by CT prior to delivery of BP-Au NPs (Figure 6a). After delivery of BP-Au NPs, the X-ray attenuation of microcalcifications containing 0.5 mg/mL

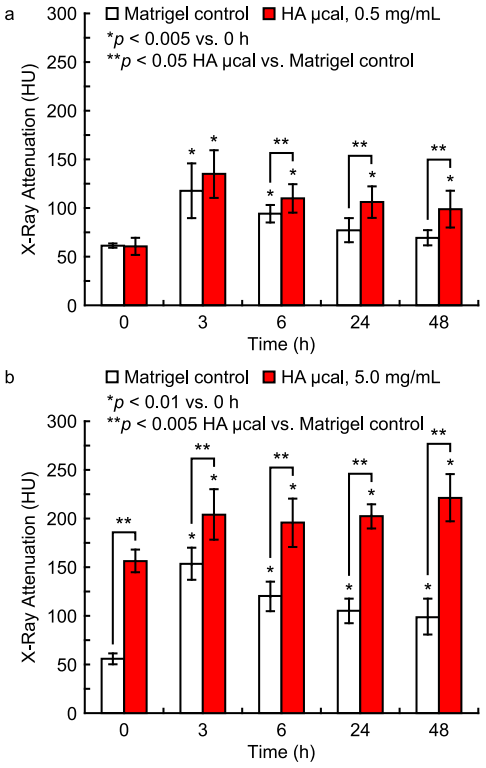

Figure 6. X-ray attenuation (HU) measured *in vivo* by CT for microcalcifications containing (a) 0.5 mg/mL and (b) 5.0 mg/mL HA compared to contralateral Matrigel controls before (0 h) and longitudinally at 3, 6, 24, and 48 h after delivery of BP-Au NPs. Error bars show one standard deviation of the mean (n = 5/group). Prior to delivery of BP-Au NPs (0 h), the X-ray attenuation exhibited by microcalcifications containing (a) 0.5 mg/mL HA was not significantly different from Matrigel controls (p = 0.85, paired t-test), whereas the X-ray attenuation exhibited by microcalcifications containing (b) 5.0 mg/mL HA was significantly greater than Matrigel controls (*p < 0.005, paired t-test). After delivery of BP-Au NPs, the X-ray attenuation of microcalcifications containing (a) 0.5 mg/mL HA (*p < 0.005, t-test) and (b) 5.0 mg/mL HA (*p < 0.01, t-test) were increased at all time points compared to prior to delivery of BP-Au NPs (0 h). The X-ray attenuation of microcalcifications containing (a) 0.5 mg/mL and (b) 5.0 mg/mL HA was greater than Matrigel controls at 24 and 48 h (p < 0.05, paired t-test) and at all time points (**p < 0.005, paired t-test), respectively. The X-ray attenuation of Matrigel controls initially increased 3 h after delivery of BP-Au NPs (a,b), but subsequently decreased at each sequential time point due to gradual clearance of BP-Au NPs.**

HA was increased at all time points (3, 6, 24, 48 h) compared to prior to delivery of BP-Au NPs (0 h) (p < 0.005, t-test). Therefore, BP-Au NPs enabled contrast-enhanced detection of microcalcifications that were otherwise below the CT detection limit. The X-ray attenuation of both the microcalcifications and Matrigel controls was initially increased at 3 h after delivery of BP-Au NPs and not statistically different (p = 0.18, paired t-test). However, by 6 h and up to 48 h after delivery of BP-Au NPs, the X-ray attenuation exhibited by HA microcalcifications was significantly greater than Matrigel controls (p < 0.05, paired t-test), resulting in a differential contrast (ΔHU) of ~30 HU at 48 h after delivery of BP-Au NPs (Figure 5a). Therefore, BP-Au NPs

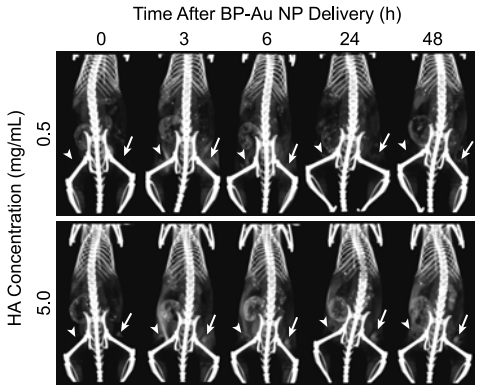

Figure 7. Representative 3D gray-scale CT images showing HA microcalcifications containing 0.5 and 5.0 mg/mL HA in left MGs (arrows) and contralateral Matrigel controls in right MGs (arrowheads) before (0 h) and longitudinally at 3, 6, 24, and 48 h after delivery of BP-Au NPs *in vivo*. Differences in X-ray attenuation between HA microcalcifications and Matrigel controls (Figure 5) were visibly apparent as BP-Au NPs were retained in the microcalcification site due to specific targeting and cleared from the Matrigel site within 48 h after delivery, demonstrating contrast-enhanced detection of microcalcifications.

targeted HA microcalcifications due to specific binding to HA crystal surfaces, resulting in increased in X-ray attenuation at the HA microcalcification site which was visibly apparent (Figure 7). Additionally, the X-ray attenuation exhibited by Matrigel controls at 24 and 48 h after delivery of BP-Au NPs was not different from Matrigel controls prior to delivery of BP-Au NPs (p > 0.01, t-test) (Figure 6a). Therefore, BP-Au NPs were cleared from Matrigel controls by 24 h after delivery due to the absence of a specific target.

Microcalcifications containing 0.5 mg/mL HA modeled a clinical situation where a microcalcification that would be missed during routine screening, due to being below the current detection limit (~0.1 mm), was detected using contrast-enhanced CT after delivery of BP-Au NPs to the site. Therefore, targeted BP-Au NPs enabled improved sensitivity for the detection of microcalcifications. BP-Au NPs were retained in HA microcalcifications and cleared from the surrounding tissue. The ability to significantly improve sensitivity for the detection of small microcalcifications of low HA concentration is very promising as it indicates that BP-Au NPs exhibited highly efficient targeting *in vivo* due to a high binding affinity for calcium on HA crystal surfaces.[31] The total number of available binding sites is decreased with decreased HA concentration requiring that a higher proportion of binding sites are filled in order to achieve a sufficient mass concentration of Au for contrast-enhanced detection. This is an inherent challenge to achieving a sufficient Au mass concentration when targeting low levels of receptors, antibodies, or microcalcifications with functionalized Au NPs.[41]

The lower limit for contrast-enhanced detection of microcalcifications, and more importantly, the minimum microcalcification burden for breast cancer

diagnosis are not yet known. While this study demonstrated success in detecting microcalcifications containing 0.5 mg/mL HA, which were previously shown to be less than 0.1 mm in size using micro-CT,[29] detection will become increasingly difficult for further decreases in the size and concentration of HA microcalcifications. Additional improvements in sensitivity could be achieved using Au NPs of larger size, which have been shown to enable targeted delivery of a greater mass concentration of BP-Au NPs per mass of HA *in vitro*[32] and greater contrast enhancement after targeted delivery *in vivo*,[22] compared to smaller Au NPs. Note, however, that Au NP size does not affect X-ray attenuation at the same mass concentration.[32] Thus, if the colloidal stability or transport properties of Au NPs are compromised by an increase in size, these potential improvements in sensitivity will not be realized.

The X-ray attenuation of microcalcifications containing 5.0 mg/mL HA was significantly greater than Matrigel controls prior to delivery of BP-Au NPs and at each time point after delivery of BP-Au NPs ($p < 0.005$, paired *t*-test) (Figure 6b). After delivery of BP-Au NPs, the X-ray attenuation of microcalcifications containing 5.0 mg/mL HA was increased at all time points compared to prior to BP-Au NP delivery ($p < 0.01$, *t*-test). Therefore, BP-Au NPs provided additional contrast enhancement for microcalcifications that were already above the CT detection limit. The X-ray attenuation of Matrigel controls initially increased 3 h after delivery of BP-Au NPs but subsequently decreased at each sequential time point due to gradual clearance of BP-Au NPs in the absence of a specific target (Figure 6b). Therefore, BP-Au NPs targeted microcalcifications due to specific binding to HA crystal surfaces, resulting in increased in X-ray attenuation at the microcalcification site, which was visibly apparent (Figure 7). The X-ray attenuation exhibited by Matrigel controls 48 h after delivery of BP-Au NPs remained greater than prior to delivery of BP-Au NPs ($p > 0.01$, *t*-test) (Figure 6a), indicating that BP-Au NPs were not yet completely cleared from the site and additional time might be required. Nonetheless, the differential contrast (ΔHU) between microcalcifications and Matrigel controls was ~100 HU prior to delivery of BP-Au NPs and increased to ~135 HU 48 h after delivery of BP-Au NPs.

Microcalcifications containing 5.0 mg/mL HA modeled a clinical situation where a suspicious lesion observed during routine screening, which would ordinarily require a biopsy, was confirmed to be a microcalcification using contrast-enhanced CT after delivery of BP-Au NPs to the site. Therefore, targeted BP-Au NPs enabled improved specificity for the detection of microcalcifications. Clearance of BP-Au NPs from a suspicious lesion could be used to eliminate potential false positives, while retention of BP-Au NPs in a suspicious lesion could be used to confirm true positives. The ability to significantly improve specificity is very promising as unnecessary biopsies increase patient anxiety and healthcare costs,[42,43] and mammographic screening is constrained in women with radiographically dense breast tissue.[44,45]

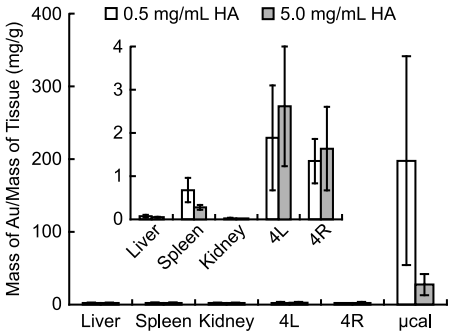

Figure 8. Biodistribution of gold 48 h after delivery of BP-Au NPs was characterized by measuring the gold concentration in organs known to accumulate Au NPs, as well as the MGs (4L, 4R) and targeted microcalcifications (μcal). Error bars show one standard deviation of the mean (μcal, $n = 3$/group; organs, $n = 5$/group). The highest concentration of gold was measured at targeted microcalcifications, while a relatively high concentration of gold remained within MGs and a much lower concentration accumulated in the liver and spleen.

A limitation of this study was the low background intensity and low variability exhibited by the MGs of wildtype mice relative to human breast tissue on mammograms. The level of contrast enhancement, or signal-to-noise ratio, is decreased with increased tissue density. The accuracy of mammography is also decreased in women with radiographically dense breast tissue,[44] while breast density is associated with an increased risk of cancer.[45] Therefore, the detection of microcalcifications in radiographically dense breast tissue is a challenge of great clinical importance. Furthermore, radiographic density varies greatly between women,[46] and this variability is important in determining the level of contrast enhancement required to detect microcalcifications. Therefore, we are actively developing a murine model of radiographically dense tissue in order to further investigate the efficiency of BP-Au NPs for detecting microcalcifications within tissues exhibiting a higher background intensity and greater variability. Nonetheless, this study demonstrated the important finding that BP-Au NPs enabled contrast-enhanced detection of HA microcalcifications *in vivo*.

***In Vivo* Biodistribution of BP-Au NPs.** The *in vivo* biodistribution of BP-Au NPs was investigated 48 h after intramammary delivery by measuring the level of gold in organs known to accumulate Au NPs,[47] as well as the MGs and targeted microcalcifications. BP-Au NPs were detected in the liver, kidneys, and spleen, but the concentration was much lower than MGs and microcalcifications (Figure 8). Therefore, the relatively high concentration of gold accumulated in microcalcifications provided further evidence for the high binding

affinity of BP-Au NPs to HA *in vivo*. The concentration of gold measured in the liver, spleen, kidneys, MGs, and microcalcifications corresponded to approximately 2.5, < 1, < 0.2, 14, and 0.3%, respectively, of the total initial dose of gold delivered. Thus, only a small fraction of the dose was needed to target microcalcifications for contrast-enhanced detection. The largest fraction of the initial dose remained in the mammary tissue, and relatively small fractions of the initial dose were accumulated in the liver and spleen. The total mass of gold detected in the liver, kidneys, and spleen was similar compared to previous studies which delivered a similar dose of Au NPs by intratumoral injection and was much lower compared to previous studies which delivered a similar dose of Au NPs by intravenous injection.[25,27]

Mice did not exhibit any signs of illness up to 48 h after delivery of BP-Au NPs. However, a more complete assessment of toxicity at longer time points is necessary in the future, including histological evaluation of specific tissues (liver, spleen, MGs). Nonetheless, the administered dose in this study (80 mg/kg) was 1 order of magnitude lower than doses used in previous studies (~440−2700 mg/kg) that demonstrated enhanced-contrast and no toxicity when using Au NPs as an X-ray contrast agent *in vivo*.[13−15]

Intramammary injections were used in this study to ensure that BP-Au NPs were delivered to microcalcifications. These injections were similar to intratumoral injections, which have been investigated as a potential delivery mode for tumor-targeted Au NPs.[25,48,49] Intratumoral injections were shown to increase the mass concentration of Au NPs in a tumor and increase the differential signal between the tumor and surrounding tissue. Additionally, and perhaps more importantly, intratumoral injections also decreased the overall distribution of Au NPs into other organs. For example, the mass of Au NPs in the spleen after an intratumoral injection was 10 times lower than after intravascular injection.[48] However, the benefit of an intratumoral or intramammary injection may be diminished when the location of a tumor or microcalcification, respectively, is not visible or known prior to injection. Therefore, intravascular delivery of BP-Au NPs will be the focus of continued investigation.

CONCLUSIONS

Bisphosphonate-functionalized gold nanoparticles (BP-Au NPs) were investigated for *in vivo* targeted delivery and contrast-enhanced detection of microcalcifications using computed tomography (CT). A murine model was developed for precise, *a priori* control over the level of microcalcification burden by injecting varying concentrations of HA crystals in a Matrigel carrier into mammary glands *in vivo*. The measured X-ray attenuation of microcalcifications containing varying HA concentrations demonstrated that the model was reproducible and able to recapitulate varying levels of microcalcification burden, including levels undetectable by CT at a clinically relevant resolution and in the absence of contrast enhancement. Based on the model characterization, two HA concentrations were chosen to mimic two levels of microcalcification burden modeling (1) microcalcifications below the CT detection limit which could be missed during routine screening (sensitivity) and (2) microcalcifications above the detection limit but difficult to distinguish from other structures of the breast (specificity). BP-Au NPs provided enhanced-contrast for the detection of microcalcifications that were otherwise below the CT detection limit, due to targeting HA crystals. Therefore, targeted BP-Au NPs enabled improved sensitivity for the detection of microcalcifications. BP-Au NPs targeted HA microcalcifications due to specific binding to HA crystal surfaces, resulting in contrast between the HA microcalcification site and surrounding tissue which was visibly apparent (~30−135 HU) within 2 days after delivery. In contrast, BP-Au NPs were mostly cleared from mammary tissue within 2 days after delivery due to the absence of a specific target. Therefore, targeted BP-Au NPs also enabled improved specificity for the detection of microcalcifications. The results of this study suggest that BP-Au NPs have potential as a targeted X-ray contrast agent for the detection of microcalcifications to improve radiographic screening for breast cancer.

METHODS

Preparation of BP-Au NPs. Au NPs were synthesized to a mean particle diameter of ~13 nm and gold concentration of ~0.5 mM in deionized (DI) water using the citrate reduction method. Briefly, 0.1 g of gold(III) chloride trihydrate ($HAuCl_4 \cdot 3H_2O$, ≥99.9%, Sigma-Aldrich, St. Louis, MO) was added to 500 mL of DI water and brought to a boil under stirring. Once boiling, 0.5 g of trisodium citrate dihydrate ($Na_3C_6H_5O_7 \cdot 2H_2O$, ACS reagent, >99%, Sigma-Aldrich) was added. The solution was boiled for 20 min before removing heat, stirring overnight, and readjusting the solution volume back to 500 mL after reaching ambient temperature, as previously described in detail.[30,31] Prior to bisphosphonate (BP) surface functionalization, 240 mL of as-synthesized Au NPs were mixed with 2 mL of 10 wt % poly(vinyl alcohol) (PVA 10−98, 61 000 Da, Fluka, St. Louis, MO) and 5.8 g of ion-exchange resin (Dowex Marathon, MR-3, Sigma-Aldrich) to remove excess ions. Au NPs were surface functionalized by mixing 250 mL of PVA-Au NPs with 4 mL of 0.01 M alendronate sodium trihydrate ($C_4H_{12}NaNO_7P_2 \cdot 3H_2O$, ≥97%, Sigma-Aldrich), which provided a primary amine for binding gold opposite a BP functional group for targeting calcium in HA, and excess BP molecules were removed by dialysis (Spectra/Por, MWCO = 3500 Da, Spectrum Laboratories, Rancho Dominquez, CA) against DI water for 3 d, changing the water at least 3 times daily.[30,31] For the *in vivo* delivery of BP-Au NPs, as-synthesized BP-Au NPs were concentrated by centrifugation (Sorvall RD 6 Plus, Thermo Scientific Corporation, Waltham, MA) using molecular weight cutoff filters (Amicon Ultra-15 10k, Millipore Corporation, Billerica, MA) for 30 min at 1485g to reach a final gold concentration

of ~50 mM (~9.8 mg/mL). Concentrated solutions of BP-Au NPs were stored in low binding Eppendorf tubes (Protein LoBind Tube 1.5 mL, Eppendorf, Hamburg, Germany) and sterilized under UV-light[50] for at least 24 h prior to administration *in vivo*.

Characterization of BP-Au NPs. Gold concentrations in as-synthesized and concentrated BP-Au NP solutions were measured using inductively coupled plasma-optical emission spectroscopy (ICP-OES, Optima 8000, PerkinElmer, Inc., Waltham, MA) after acidifying with 3% aqua regia (3 HCl:1 HNO_3). Calibration curves were created by diluting certified standard gold solutions (Assurance grade, SPEX CertiPrep, Metuchen, NJ). The mean particle diameter, mean hydrodynamic diameter, colloidal stability in physiological media, and bisphosphonate surface density were all characterized for concentrated BP-Au NPs and compared to previous results for as-synthesized BP-Au NPs.[29−32] The mean particle diameter was measured using transmission electron microscopy (TEM, FEI Titan 80−300, Hillsboro, OR) at 80 kV accelerating voltage. TEM specimens were prepared by evaporating drops pipetted from BP-Au NP solutions on carbon-coated grids. The mean particle diameter was measured from a total of 100 randomly selected particles. The hydrodynamic diameter was measured using dynamic light scattering (DLS, Zetasizer Nano ZS90, Malvern Instruments Ltd., Worcestershire, UK), after diluting concentrated BP-Au NPs in DI water to a final gold concentration of ~0.5 μM, and reported as the mean of three samples. Colloidal stability was verified by measuring the surface plasmon resonance peak using ultraviolet−visible (UV−vis) spectroscopy (Nanodrop 200C, Thermo Scientific, Wilmington, DE) after diluting concentrated BP-Au NPs in DI water to a final gold concentration of 0.5 mM.

Murine Model of Breast Microcalcifications. Mature 10- to 14-week-old nulliparous, female FVB mice (Charles River Laboratories International, Inc., Wilmington, MA) were used to develop an *in vivo* model of microcalcifications in mammary tissue. All studies were approved by the Institutional Animal Care and Use Committee at the University of Notre Dame and were conducted in accordance with the guidelines of the U.S. Public Health Service Policy for Humane Care and Use of Laboratory Animals. All efforts were made to minimize suffering of the mice. The skin of anesthetized mice was prepared for injection by applying a small drop of depilatory cream for 10 s to remove the fur surrounding the nipple area of the left and right number 4 mammary glands (MGs). Sterile ethanol pads were then used to remove the depilatory cream and clean the skin. Microcalcifications were created by injecting the right number 4 MG of anesthetized mice with 50 μL of Matrigel (BD Matrigel, BD Sciences, Bedford, MA), a hydrogel comprised of extracellular matrix proteins, containing HA crystals at concentrations of 0, 0.5, 5.0, and 25 mg/mL HA (n = 8/group) (Figure 1b). HA crystals were synthesized using the chelate decomposition method,[51] and exhibited an elongated whisker-like morphology (~18 × 2 μm) and a specific surface area of 5.63 m^2/g.[31]

Microcalcifications Labeled by BP-Au NPs *in Vitro*. The left number 4 MG of the same mice described above was injected with the same concentration of HA crystals which were labeled by BP-Au NPs *in vitro* with either a low (10 mg/L) (n = 3/group) or high (54 mg/L) (n = 5/group) concentration of BP-Au NPs (Figure 1b). HA-Matrigel compositions were prepared by labeling HA crystals with BP-Au NPs prior to mixing with Matrigel.[29] HA concentrations of 0.5, 5.0, and 25 mg/mL were incubated in DI water containing either 10 mg/L (0.051 mM) or 54 mg/L (0.274 mM) BP-Au NPs for 24 h to allow for maximum binding of the available BP-Au NPs to the HA crystals.[31] Each HA concentration was exposed to the same BP-Au NP concentration for the same length of time. Unbound BP-Au NPs were separated from HA crystals by centrifugation at ~700g for 2 min. HA crystals labeled by BP-Au NPs were collected using 0.45 μm filter paper (Nylaflo, Pall Corporation, Ann Arbor, MI), rinsed with 10 mL of DI water, dried overnight in an oven at 37 °C, and stored under vacuum until mixed with Matrigel.

The percent of BP-Au NPs bound to HA crystals was measured as the concentration of unbound BP-Au NPs subtracted from the initial BP-Au NP concentration, divided by the initial BP-Au NP concentration. The initial gold concentration and the concentration of unbound BP-Au NPs were measured using ICP-OES, as described above. The mass of BP-Au NPs bound per mass of HA (mg Au/g HA) was calculated using the mass of HA added. The mean (±standard deviation) percent of BP-Au NPs bound and mass of BP-Au NPs bound per mass of HA were measured from three samples for each HA concentration.

Targeted Delivery of BP-Au NPs to Microcalcifications *in Vivo*. HA microcalcifications were created in the fat pad of the left number 4 MG of anesthetized female mice, as described above. Two HA concentrations were chosen to model microcalcifications that were undetectable (0.5 mg/mL) and detectable (5.0 mg/mL) by CT in the absence of contrast enhancement. The left number 4 MG was injected with 50 μL of Matrigel containing 0.5 or 5.0 mg/mL HA crystals; the right MG was injected with 50 μL of Matrigel alone as a contralateral control (n = 5/HA concentration) (Figure 1c). BP-Au NPs were administered to anesthetized mice by intramammary delivery 24 h after creating microcalcifications in MGs at a total dose of 2 mg Au per mouse from 100 μL of 50 mM BP-Au NP solutions injected into each MG.

***In Vivo* CT and Radiography.** Twenty-four hours after creating microcalcifications, anesthetized mice were imaged *in vivo* by computed tomography (CT, Albira, Bruker Biosciences Corporation, Billerica, MA) at 45 kVp, 400 μA, 250 ms integration time and 125 μm resolution for 600 slices with a 0.5 mm aluminum filter. Mice were also imaged by planar radiography (In Vivo Xtreme, Bruker) at 20 kVp with a 0.1 mm aluminum filter and 10 s exposure time immediately after CT. For planar radiography, the skin and MG were pulled away from the body cavity and gently fixed to the specimen plate by tape.[52] For targeted delivery experiments, mice were imaged immediately prior to delivery of BP-Au NPs (0 h) and longitudinally at 3, 6, 24, and 48 h after delivery of BP-Au NPs. Internal calibrations for air and water controls were included in the first and last CT scan performed each day.

***In Vivo* CT X-ray Attenuation Measurements.** X-ray attenuation was measured within a volume of interest (VOI) surrounding the number 4 MG and reported in Hounsfield units (HU) as the mean (±standard deviation) for each group for the initial murine model characterization, including microcalcifications labeled by BP-Au NPs *in vitro*. The VOI was created manually at the margin between the enhanced-contrast of HA-Matrigel compositions and the surrounding adipose tissue in the MG. The mean (±standard deviation) VOI for this analysis was 1.6 (0.2) mm^3. For the *in vivo* targeted delivery experiments, CT images acquired immediately prior to delivery of BP-Au NPs (0 h) were used to determine the VOI for each animal by the same method described above. This VOI was then mapped onto subsequent CT images acquired at each time point after delivery of BP-Au NPs in the same mouse to ensure consistency. The mean (±standard deviation) VOI for this analysis was 2.0 (0.4) mm^3.

***In Vivo* Biodistribution.** Mice were sacrificed 48 h after delivery of BP-Au NPs. The liver, kidney, spleen, and both number 4 MGs were dissected. Microcalcifications created within left MGs were also dissected and analyzed separately. Organs were dried overnight in an oven at 37 °C, massed, and digested in 4 mL of aqua regia for 24 h. Microcalcifications were digested in 0.5 mL of aqua regia for 24 h. The mass of Au in each sample was measured using ICP-OES, as described above. Tissues from three additional FVB mice were also collected and analyzed as controls.

Statistical Methods. For the initial murine model characterization, including microcalcifications labeled by BP-Au NPs *in vitro*, differences in the X-ray attenuation of HA concentrations and differences in the binding of BP-Au NPs to HA crystals were examined using two-way analysis of variance (ANOVA), and *post hoc* comparisons were performed using unpaired Student's *t*-tests. Differences in the X-ray attenuation of HA microcalcifications in the right MG and HA microcalcifications labeled by BP-Au NPs *in vitro* in the left MG of each mouse were examined using paired *t*-tests. For the *in vivo* targeted delivery experiments, changes in the X-ray attenuation with time for each group (HA microcalcification or Matrigel control) were examined using one-way ANOVA and *post hoc* comparisons were performed using unpaired Student's *t*-tests. Differences in the X-ray attenuation of Matrigel controls in the right MG and HA

microcalcifications in the left MG of each mouse were examined using paired *t*-tests. The level of significance for all tests was set at $p < 0.05$.

Conflict of Interest: The authors declare no competing financial interest.

Acknowledgment. This work was supported by a Seeding Research in Cancer Grant from the St. Joseph Regional Medical Center in Mishawaka, IN, and an Engineering Novel Solutions to Cancer's Challenges at the Interdisciplinary Interface Training Grant from the Walther Cancer Foundation. We acknowledge the Freimann Life Science Center at the University of Notre Dame for the care of animals; the Notre Dame Integrated Imaging Facility for the use of CT, radiography, and electron microscopy; and the Center for Environmental Science and Technology at the University of Notre Dame for use of ICP-OES.

REFERENCES AND NOTES

1. Etzioni, R.; Urban, N.; Ramsey, S.; McIntosh, M.; Schwartz, S.; Reid, B.; Radich, J.; Anderson, G.; Hartwell, L. The Case for Early Detection. *Nat. Rev. Cancer* **2003**, *3*, 243–252.
2. Smith, R. A.; Duffy, S. W.; Tabár, L. Breast Cancer Screening: The Evolving Evidence. *Oncology* **2012**, *26*, 471–486.
3. Weissleder, R.; Pittet, M. J. Imaging in the Era of Molecular Oncology. *Nature* **2008**, *452*, 580–589.
4. Elmore, J. G.; Armstrong, K.; Lehman, C. D.; Fletcher, S. W. Screening for Breast Cancer. *JAMA, J. Am. Med. Assoc.* **2005**, *293*, 1245–1256.
5. Tabár, L.; Fagerberg, C. J.; Gad, A.; Baldetorp, L.; Holmberg, L. H.; Gröntoft, O.; Ljungquist, U.; Lundström, B.; Månson, J. C.; Eklund, G. Reduction in Mortality From Breast Cancer After Mass Screening with Mammography. Randomised Trial From the Breast Cancer Screening Working Group of the Swedish National Board of Health and Welfare. *Lancet* **1985**, *325*, 829–832.
6. Tabár, L.; Vitak, B.; Chen, T. H.-H.; Yen, A. M.-F.; Cohen, A.; Tot, T.; Chiu, S. Y.-H.; Chen, S. L.-S.; Fann, J. C.-Y.; Rosell, J.; et al. Swedish Two-County Trial: Impact of Mammographic Screening on Breast Cancer Mortality During Three Decades. *Radiology* **2011**, *260*, 658–663.
7. Morgan, M. P.; Cooke, M. M.; McCarthy, G. M. Microcalcifications Associated with Breast Cancer: An Epiphenomenon or Biologically Significant Feature of Selected Tumors? *J. Mammary Gland Biol. Neoplasia* **2005**, *10*, 181–187.
8. Cheng, H. D.; Cai, X.; Chen, X.; Hu, L.; Lou, X. Computer-Aided Detection and Classification of Microcalcifications in Mammograms: A Survey. *Pattern Recogn.* **2003**, *36*, 2967–2991.
9. Gülsün, M.; Demirkazk, F. B.; Aryürek, M. Evaluation of Breast Microcalcifications According to Breast Imaging Reporting and Data System Criteria and Le Gal's Classification. *Eur. J. Radiol.* **2003**, *47*, 227–231.
10. Frappart, L.; Remy, I.; Lin, H. C.; Bremond, A.; Raudrant, D.; Grousson, B.; Vauzelle, J. L. Different Types of Microcalcifications Observed in Breast Pathology. *Virchows Arch. A: Pathol. Anat. Histol.* **1986**, *410*, 179–187.
11. Büsing, C. M.; Keppler, U.; Menges, V. Differences in Microcalcification in Breast Tumors. *Virchows Arch. A: Pathol. Anat. Histol.* **1981**, *393*, 307–313.
12. Haka, A. S.; Shafer-Peltier, K. E.; Fitzmaurice, M.; Crowe, J.; Dasari, R. R.; Feld, M. S. Identifying Microcalcifications in Benign and Malignant Breast Lesions by Probing Differences in Their Chemical Composition Using Raman Spectroscopy. *Cancer Res.* **2002**, *62*, 5375–5380.
13. Hainfeld, J. F.; Slatkin, D. N.; Focella, T. M.; Smilowitz, H. M. Gold Nanoparticles: A New X-Ray Contrast Agent. *Br. J. Radiol.* **2006**, *79*, 248–253.
14. Kim, D.; Park, S.; Lee, J. H.; Jeong, Y. Y.; Jon, S. Antibiofouling Polymer-Coated Gold Nanoparticles as a Contrast Agent for *In Vivo* X-Ray Computed Tomography Imaging. *J. Am. Chem. Soc.* **2007**, *129*, 7661–7665.
15. Cai, Q.-Y.; Kim, S. H.; Choi, K. S.; Kim, S. Y.; Byun, S. J.; Kim, K. W.; Park, S. H.; Juhng, S. K.; Yoon, K.-H. Colloidal Gold Nanoparticles as a Blood-Pool Contrast Agent for X-Ray Computed Tomography in Mice. *Invest. Radiol.* **2007**, *42*, 797–806.
16. Sperling, R. A.; Rivera Gil, P.; Zhang, F.; Zanella, M.; Parak, W. J. Biological Applications of Gold Nanoparticles. *Chem. Soc. Rev.* **2008**, *37*, 1896–1908.
17. Popovtzer, R.; Agrawal, A.; Kotov, N. A.; Popovtzer, A.; Balter, J.; Carey, T. E.; Kopelman, R. Targeted Gold Nanoparticles Enable Molecular CT Imaging of Cancer. *Nano Lett.* **2008**, *8*, 4593–4596.
18. Aydogan, B.; Li, J.; Rajh, T.; Chaudhary, A.; Chmura, S. J.; Pelizzari, C.; Wietholt, C.; Kurtoglu, M.; Redmond, P. AuNP-DG: Deoxyglucose-Labeled Gold Nanoparticles as X-Ray Computed Tomography Contrast Agents for Cancer Imaging. *Mol. Imaging Biol.* **2010**, *12*, 463–467.
19. Li, J.; Chaudhary, A.; Chmura, S. J.; Pelizzari, C.; Rajh, T.; Wietholt, C.; Kurtoglu, M.; Aydogan, B. A Novel Functional CT Contrast Agent for Molecular Imaging of Cancer. *Phys. Med. Biol.* **2010**, *55*, 4389–4397.
20. Kim, D.; Jeong, Y. Y.; Jon, S. A Drug-Loaded Aptamer-Gold Nanoparticle Bioconjugate for Combined CT Imaging and Therapy of Prostate Cancer. *ACS Nano* **2010**, *4*, 3689–3696.
21. Chanda, N.; Kattumuri, V.; Shukla, R.; Zambre, A.; Katti, K.; Upendran, A.; Kulkarni, R. R.; Kan, P.; Fent, G. M.; Casteel, S. W.; et al. Bombesin Functionalized Gold Nanoparticles Show *In Vitro* and *In Vivo* Cancer Receptor Specificity. *Proc. Natl. Acad. Sci. U.S.A.* **2010**, *107*, 8760–8765.
22. Eck, W.; Nicholson, A. I.; Zentgraf, H.; Semmler, W.; Bartling, S. Anti-CD4-Targeted Gold Nanoparticles Induce Specific Contrast Enhancement of Peripheral Lymph Nodes in X-Ray Computed Tomography of Live Mice. *Nano Lett.* **2010**, *10*, 2318–2322.
23. Reuveni, T.; Motiei, M.; Romman, Z.; Popovtzer, A.; Popovtzer, R. Targeted Gold Nanoparticles Enable Molecular CT Imaging of Cancer: An *In Vivo* Study. *Int. J. Nanomed.* **2011**, *6*, 2859–2864.
24. Hainfeld, J. F.; O'Connor, M. J.; Dilmanian, F. A.; Slatkin, D. N.; Adams, D. J.; Smilowitz, H. M. Micro-CT Enables Microlocalisation and Quantification of Her2-Targeted Gold Nanoparticles Within Tumour Regions. *Br. J. Radiol.* **2011**, *84*, 526–533.
25. Wang, H.; Zheng, L.; Peng, C.; Shen, M.; Shi, X.; Zhang, G. Folic Acid-Modified Dendrimer-Entrapped Gold Nanoparticles as Nanoprobes for Targeted CT Imaging of Human Lung Adenocarcinoma. *Biomaterials* **2013**, *34*, 470–480.
26. Liu, H.; Xu, Y.; Wen, S.; Chen, Q.; Zheng, L.; Shen, M.; Zhao, J.; Zhang, G.; Shi, X. Targeted Tumor Computed Tomography Imaging Using Low-Generation Dendrimer-Stabilized Gold Nanoparticles. *Chem.—Eur. J.* **2013**, *19*, 6409–6416.
27. Chen, Q.; Li, K.; Wen, S.; Liu, H.; Peng, C.; Cai, H.; Shen, M.; Zhang, G.; Shi, X. Targeted CT/MR Dual Model Imaging of Tumors Using Multifunctional Dendrimer-Entrapped Gold Nanoparticles. *Biomaterials* **2013**, *34*, 5200–5209.
28. Sun, I.-C.; Na, J. H.; Jeong, S. Y.; Kim, D.-E.; Kwon, I. C.; Choi, K.; Ahn, C.-H.; Kim, K. Biocompatible Glycol Chitosan-Coated Gold Nanoparticles for Tumor-Targeting CT Imaging. *Pharm. Res.* **2013**in press.
29. Cole, L. E.; Vargo-Gogola, T.; Roeder, R. K. Bisphosphonate-Functionalized Gold Nanoparticles for Contrast-Enhanced X-Ray Detection of Breast Microcalcifications. *Biomaterials* **2014**, *35*, 2312–2321.
30. Ross, R. D.; Cole, L. E.; Roeder, R. K. Relative Binding Affinity of Carboxylate-, Phosphonate-, and Bisphosphonate-Functionalized Gold Nanoparticles Targeted to Damaged Bone Tissue. *J. Nanopart. Res.* **2012**, *14*, 1175.
31. Ross, R. D.; Roeder, R. K. Binding Affinity of Surface Functionalized Gold Nanoparticles to Hydroxyapatite. *J. Biomed. Mater. Res.* **2011**, *99A*, 58–66.
32. Ross, R. D.; Cole, L. E.; Tilley, J. M. R.; Roeder, R. K. Effect of Functionalized Gold Nanoparticle Size on X-Ray Attenuation and Binding Affinity to Hydroxyapatite. *Chem. Mater.* **2014**, *26*, 1187–1194.
33. Cox, R. F.; Hernandez-Santana, A.; Ramdass, S.; McMahon, G.; Harmey, J. H.; Morgan, M. P. Microcalcifications in Breast Cancer: Novel Insights Into the Molecular Mechanism and

Functional Consequence of Mammary Mineralisation. *Br. J. Cancer* **2012**, *106*, 525–537.
34. Liu, F.; Bloch, N.; Bhushan, K. R.; de Grand, A. M.; Tanaka, E.; Solazzo, S.; Mertyna, P. M.; Goldberg, N.; Frangioni, J. V.; Lenkinski, R. E. Humoral Bone Morphogenetic Protein-2 Is Sufficient for Inducing Breast Cancer Microcalcification. *Mol. Imaging* **2008**, *7*, 175–186.
35. Liu, F.; Misra, P.; Lunsford, E. P.; Vannah, J. T.; Liu, Y.; Lenkinski, R. E.; Frangioni, J. V. A Dose- and Time-Controllable Syngeneic Animal Model of Breast Cancer Microcalcification. *Breast Cancer Res. Tr.* **2010**, *122*, 87–94.
36. Inoue, K.; Liu, F.; Hoppin, J.; Lunsford, E. P.; Lackas, C.; Hesterman, J.; Lenkinski, R. E.; Fujii, H.; Frangioni, J. V. High-Resolution Computed Tomography of Single Breast Cancer Microcalcifications *In Vivo*. *Mol. Imaging* **2011**, *10*, 295–204.
37. Karssemeijer, N.; Frieling, J.; Hendrick, J. Spatial Resolution in Digital Mammography. *Invest. Radiol.* **1993**, *28*, 413–419.
38. Kwan, A. L. C.; Boone, J. M.; Yang, K.; Huang, S.-Y. Evaluation of the Spatial Resolution Characteristics of a Cone-Beam Breast CT Scanner. *Med. Phys.* **2007**, *34*, 275–281.
39. Galper, M. W.; Saung, M. T.; Fuster, V.; Roessl, E.; Thran, A.; Proksa, R.; Fayad, Z. A.; Cormode, D. P. Effect of Computed Tomography Scanning Parameters on Gold Nanoparticle and Iodine Contrast. *Invest. Radiol.* **2012**, *47*, 475–481.
40. Krause, W. Delivery of Diagnostic Agents in Computed Tomography. *Adv. Drug Delivery Rev.* **1999**, *37*, 159–173.
41. Sinha, R.; Kim, G. J.; Nie, S.; Shin, D. M. Nanotechnology in Cancer Therapeutics: Bioconjugated Nanoparticles for Drug Delivery. *Mol. Cancer Ther.* **2006**, *5*, 1909–1917.
42. Brodersen, J.; Siersma, V. D. Long-Term Psychosocial Consequences of False-Positive Screening Mammography. *Ann. Fam. Med.* **2013**, *11*, 106–115.
43. Chubak, J.; Boudreau, D. M.; Fishman, P. A.; Elmore, J. G. Cost of Breast-Related Care in the Year Following False Positive Screening Mammograms. *Med. Care* **2010**, *48*, 815–820.
44. Kolb, T. M.; Lichy, J.; Newhouse, J. H. Comparison of the Performance of Screening Mammography, Physical Examination, and Breast US and Evaluation of Factors That Influence Them: An Analysis of 27,825 Patient Evaluations. *Radiology* **2002**, *225*, 165–175.
45. Boyd, N. F.; Guo, H.; Martin, L. J.; Sun, L.; Stone, J.; Fishell, E.; Jong, R. A.; Hislop, G.; Chiarelli, A.; Minkin, S.; Yaffe, M. J. Mammographic Density and the Risk and Detection of Breast Cancer. *New. Engl. J. Med.* **2007**, *356*, 227–236.
46. Mousa, D. S. A.; Ryan, E. A.; Mello-Thoms, C.; Brennan, P. C. What Effect Does Mammographic Breast Density Have on Lesion Detection in Digital Mammography?. *Clin. Radiol.* **2014**, *69*, 333–341.
47. Khlebtsov, N.; Dykman, L. Biodistribution and Toxicity of Engineered Gold Nanoparticles: A Review of *In Vitro* and *In Vivo* Studies. *Chem. Soc. Rev.* **2011**, *40*, 1647–1671.
48. Chattopadhyay, N.; Fonge, H.; Cai, Z.; Scollard, D.; Lechtman, E.; Done, S. J.; Pignol, J.-P.; Reilly, R. M. Role of Antibody-Mediated Tumor Targeting and Route of Administration in Nanoparticle Tumor Accumulation *In Vivo*. *Mol. Pharmaceutics* **2012**, *9*, 2168–2179.
49. Yao, L.; Daniels, J.; Moshnikova, A.; Kuznetsov, S.; Ahmed, A.; Engelman, D. M.; Reshetnyak, Y. K.; Andreev, O. A. pHLIP Peptide Targets Nanogold Particles to Tumors. *Proc. Natl. Acad. Sci. U.S.A.* **2013**, *110*, 465–470.
50. França, Á.; Pelaz, B.; Moros, M.; Sánchez-Espinel, C.; Hernández, A.; Fernández-Lopez, C.; Grazú, V.; de la Fuente, J.; Pastoriza-Santos, I.; Liz-Marzán, L. M.; González-Fernández, Á. Sterilization Matters: Consequences of Different Sterilization Techniques on Gold Nanoparticles. *Small* **2010**, *6*, 89–95.
51. Roeder, R. K.; Converse, G. L.; Leng, H.; Yue, W. Kinetic Effects on Hydroxyapatite Whiskers Synthesized by the Chelate Decomposition Method. *J. Am. Ceram. Soc.* **2006**, *89*, 2096–2104.
52. Hariri, M.; Wood, G. A.; DiGrappa, M. A.; MacPherson, M.; Backman, S. A.; Yaffe, M. J.; Mak, T. W.; Boyd, N. F.; Khokha, R. Experimental Manipulation of Radiographic Density in Mouse Mammary Gland. *Breast Cancer Res.* **2004**, *6*, R540–R545.